A Stochastic Model for Contact Surfaces at Polymer Interfaces Subjected to an Electric Field

Emre Kantar[a,*], Sverre Hvidsten[b], Frank Mauseth[a], Erling Ildstad[a]

[a] *Department of Electric Power Engineering, NTNU, O.S. Bragstads Plass 2E, 7491 Trondheim, Norway*
[b] *SINTEF Energy Research, Stiftelsen SINTEF, P.O. Box 4760 Torgarden, 7465 Trondheim, Norway*

Abstract

Morphology of the contact area between solid insulation materials ultimately determines the long-term electrical properties of the complete insulation system. The primary purpose of this paper is not only to propose a statistical model to scrutinize the real area of contact between solid dielectric surfaces but also to verify and correlate the model outputs with experiments. The model computes real area of contact, number of contact spots and average cavity size at the interface as a function of elasticity, contact force and surface roughness. Then, using the average cavity size and the Paschen's law, cavity discharge inception field (PDIE) is calculated. In the experiments, AC breakdown strength (BDS) testing of solid-solid interfaces was carried out, where cross-linked polyethylene (XLPE) samples with four different surface roughnesses were subjected to various contact pressures.

Following the increased contact force, the calculated average cavity size decreased by a factor of $4.08 - 4.82$ from the roughest to the smoothest surface, that in turn yielded increased PDIEs by a factor of $2.01 - 2.56$. Likewise, the experimentally obtained BDS values augmented by a factor of $1.4 - 1.7$ when the contact pressure was elevated from 0.5 MPa to 1.16 MPa.

A linear correlation between the PDIE and BDS was assumed, yielding a correlation coefficient varying within $0.8-1.3$. When the 90% confidence intervals were considered, the range reduced to $0.86 - 1.05$. This close affinity suggests that interfacial breakdown phenomenon is strongly governed by the cavity discharge. Hence, the proposed model is verified with experiments.

Keywords: Cables, contact surface, contact mechanics, elastic, optical microscopy, polishing, polymer, texture, XLPE.

1. Introduction

The series connection of two or more dielectric materials constitute the electrical insulation system in most high voltage apparatus. The alternating current (AC) breakdown strength (BDS) of insulation systems is limited by the lowest BDS of either the bulk insulating materials or the interface between the adjacent insulating materials. The interfacial breakdown between two solid insulating materials is complex and accounts for one of the principal modes of failure for power cable joints [1]. The interface increases the risk of tracking failure due to the local electric field enhancements caused by the imperfections at the interface such as microscopic cavities, protrusions and impurities [2–6].

Cable accessories as power cable joints, outdoor composite terminations, and subsea connectors have solid-solid interfaces, which undergo electrical stress in the course of entire service life by the tangential component of the electric field [3]. Hence, it is of paramount importance to study and identify the parameters affecting the breakdown strength of such interfaces to develop cost-effective, long-lasting, and most importantly, reliable high voltage apparatus and equipment. With this motivation, many researchers and engineers have studied polymers, as insulating materials in cable accessories to a large extent [2–7]. The impacts of contact pressure and surface roughness on the interfacial BDS were studied in [1–5], where a higher interfacial pressure and a smoother surface reportedly led to an increased tangential BDS. However, mostly only empirical studies have been performed using the complete designs of connectors, accessories, and apparatus. The polymer interfaces should be scrutinized separately and diligently by considering the contact surface texture, type of the contact (i.e., elastic or plastic), surface roughness, elasticity modulus and applied contact force. Thus, comprehensive theoretical models incorporating these parameters should be developed in addition to the experimental studies in the literature because the understanding of tribological principles dominating in solid interfaces paves the path for the successful design of advanced apparatus.

The primary motivation of this paper is to model the contact surfaces between solid materials as a function of the applied mechanical contact pressure, surface texture/roughness, and elastic modulus using the tribological principles presented in [8–15]. For this purpose, a stochastic model of multiple-asperity dry contacts

*Corresponding author. Department of Electric Power Engineering, NTNU, O.S. Bragstads Plass 2E, 7491 Trondheim, Norway.
Email address: emre.kantar@ntnu.no (Emre Kantar)

DOI: 10.1016/j.triboint.2018.03.003
Paper link: https://www.sciencedirect.com/science/article/pii/S0301679X18301403?via%3Dihub

formed at a solid-solid interface is developed in $2-D$, which estimates the average size of cavities at the given interface. Then, cavity AC partial discharge inception field (PDIE) of the average-sized cavity is calculated by employing the Paschen's law. To test the validity of the model, experiments on the tangential AC BDS of solid-solid interfaces under various contact pressure were performed. Subsequently, the correlation between the calculated PDIE values and the experimental BDS is discussed in detail. In the experiments, cross-linked polyethylene (XLPE) samples with four different surface roughnesss were used to realize the polymer interfaces since XLPE can withstand high pressures without any significant deformation over a broad contact pressure range experienced in real-life applications. Besides, XLPE is one of the most prevalent materials preferred in the cable industry and is readily available for research activities.

2. Background

2.1. Contact Surfaces of Dielectric Materials

Although cable accessories are prefabricated and pretested for partial discharges (PD), they are assembled/fitted on site under sub-optimal and less controllable conditions [3]. Assembly procedure, thus, does not incorporate an automated process under clean room conditions, which makes them somewhat vulnerable to bad installations. As a consequence, interfacial surfaces become rife with imperfections such as cavities, protrusions, and contaminants/impurities [1]. Even when the magnitude of the tangential electric field is much lower than the dielectric strength of the bulk insulation, the existence of such imperfections at the interface causes local electric field enhancements [3, 16]. They are, hence, likely to result in the initiation of PDs or surface discharges, which degrade the insulation over time and give rise to a premature failure [1–6, 17, 18].

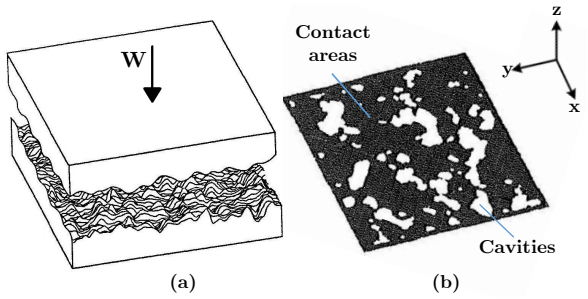

Figure 1: Schematic drawing of: (a) Two 3-D rough surfaces in contact. (b) Corresponding contact areas/spots [10].

The cavities on a solid dielectric surface have various sizes and distribution depending on the methods concerning surface polishing, manufacturing, and assembly [3]. When two nominally flat surfaces are placed in contact, surface asperities cause contact to occur at discrete contact spots whereas manifold cavities arise between the contact spots as schematically represented in Fig. 1. The real contact area, thus, is much smaller than the nominal area as illustrated. A typical cavity formed at the interface is much larger in the tangential direction (x−axis or y−axis) as delineated in Fig. 2 [10]. The parameters that influence the distribution and size of the contact spots and the cavities are discussed in the next section.

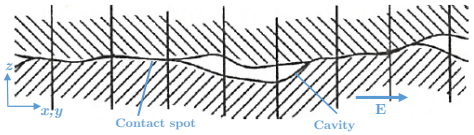

Figure 2: An illustration of the cavities at the interface in two-dimensional profile [11].

2.2. Electrical Properties of Solid-Solid Interfaces

When the interface is assembled under dry conditions, the cavities are filled with air. The applied voltage is then distributed along the strings of the cavities and contact spots. The exact size and number of the cavities are however unknown and depend heavily on the following parameters: the elasticity of the material, the applied contact pressure, and the surface roughness as depicted in Fig. 3.

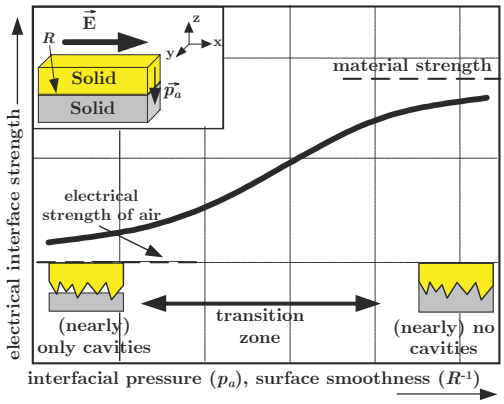

Figure 3: Tangential breakdown strength of interfaces against interface pressure and the surface roughness/smoothness [19].

The interfacial breakdown voltage and time to breakdown are very much governed by these parameters. The interfacial BDS is, for instance, slightly higher than that of air whereas it is not as strong as the bulk material strength even under a higher contact pressure or a smoother surface as shown in the Fig. 3. Besides, the increased contact pressure renders the interfacial BDS higher because the increased pressure further deforms the tips of the protrusions and makes the cavities smaller that in turn augment the interfacial BDS [19]. Likewise, smoother surfaces indicate as similar an influence on the BDS as the increased pressure, due to the mitigated cavity size at the interface. Since the dielectric strength of air is much lower than that of the bulk insulation, the dielectric breakdown will hence first occur in the air-filled cavities, and then the complete flashover follows.

2.3. Approaches to Rough Surfaces

There are various approaches to the description of rough engineering surfaces in the history of tribology, such as statistical approaches, fractal approaches, approaches based upon the surface power spectrum [20] as well as numerical deterministic roughness models [21]. One of the earliest statistical models of contact between rough elastic solids was offered by Zhuravlev (1940) [22]. Johnson (1975) [23] and Greenwood (1990) [24] are among the first scientists having cited the Zhuravlev model. With the aim of developing the Zhuravlev model, Greenwood and Williamson [12] later proposed a contact model of nominally flat surfaces, where both Gaussian and exponential distribution of the asperity peaks were tested to show that the real contact area is proportional to the applied load. More recently, Borodich's introduction to Zhuravlev's historical paper [25] highlighted that the Greenwood-Williamson's theory (1966) [12] that assumes the asperities having the same radii with various heights is a development of Zhuravlev's model for purely elastic contact published in 1940 [22]. In fact, the Greenwood and Williamson [12] modified the Zhuravlev model by covering elasto-plastic transition of asperities. On the other hand, Archard [26] worked on multilevel structure of the roughness where a sphere of radius consists of spherical protuberances whose radii are much smaller. The idea of iterative hierarchical structure of roughness was further developed in [27]. Also, Nayak [28] and Whitehouse and Archard [29] studied modeling of surfaces as random processes; however, it later turned out that the mean radius of curvature is scale dependent [20]. With the aim of providing a scale-invariant characterization of roughness to obtain the contact area more accurately, fractal approaches have been introduced more recently [20, 30, 31]. Fractal characterization supplies information of the surface roughness at all the length scales that depict the fractal behavior [31]. Several distinguished tribology researchers; however, argued that empirical fractals do not yield scale-independent parameters for description of rough surfaces [20, 32]. Thus, fractal approach is still an active area of research [20]. Approaches to surface roughness based on the surface power spectrum have also been frowned upon due to lack of mathematical justification [20].

The Greenwood and Williamson model [12] together with Bhushan's modifications [10] are adopted to develop the proposed statistical model in the next section.

3. Stochastic Modeling of Multiple-Asperity Dry Contacts of Rough Surfaces in Tribology

3.1. Statistical Analysis of Surface Contacts

If the two rough surfaces as depicted in Fig. 4, which are both nominally flat, are brought in contact until their reference planes are separated by a distance d, numerous discrete contact spots then arise at those asperities whose total heights $z_1 + z_2$ are greater than d [8–10]. Greenwood and Williamson [12] analyzed a rough surface against a smooth surface, where the contacts are either elastic or plastic, and stated that:

- the rough surface incorporates a large number of asperities, which are of spherical geometry at least near their summit;
- asperities on each surface have a constant summit radius, whereas their heights vary randomly;
- most surfaces found in engineering applications have normally distributed asperities and peak heights.

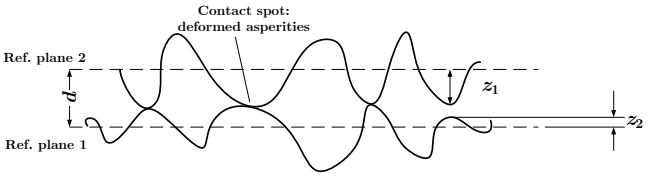

Figure 4: Contact of two rough surfaces [9].

Williamson et al. [13] addressed that preparing surfaces with cumulative processes (either single-point processes or extreme-value processes) resulted in a Gaussian-height distribution, whereas peak heights had a Gaussian distribution in all cases. On the other hand, Greenwood and Tripp [15] studied the contact surface of two rough surfaces as opposed to examining one rough surface against a nominally flat surface as performed in Greenwood and Williamson [12]. There, contact spots occur on the shoulders of the two adjacent hills since the asperity pairs are not aligned. Based on this, they discovered that as long as peak-height distribution is Gaussian, the asperity shape and whether the asperities exist on one or both surfaces are petty. In the light of this finding, Bhushan [9] addressed that the assumption of the spherical asperity tips for the sake of simplicity (first bullet point) does not affect real-area calculations. Besides, Greenwood and Tripp [15] showed that the contact of two rough surfaces could be reduced to an equivalent sum surface, consisting of a single, rough surface with a smooth rigid plane. O'Callaghan and Cameron [33] and Francis [34] also published supporting results such that the contact of two rough surfaces negligibly differs from the sum surface consisting of a smooth and an equivalent rough surface. The asperity-peak curvature, β_m of the equivalent rough surface (sum surface) is then defined as the sum of the asperities of two rough surfaces:

$$1/\beta_m = 1/\beta_{m1} + 1/\beta_{m2}. \tag{1}$$

Also, elementary statistics suggests that if the peak-height distributions of two rough surfaces are independent (as is likely when two surfaces are prepared separately) and are distributed randomly (not necessarily Gaussian) with standard deviations of the asperities σ_{p1} and σ_{p2}, the distribution of the equivalent rough surface will have a standard deviation of σ_p [9, 10]:

$$\sigma_p = \sqrt{\sigma_{p1}^2 + \sigma_{p2}^2}\,. \tag{2}$$

As the contact pressure between the two contacting samples is applied, elastic deformation initially takes place as a function of their Young's moduli of elasticity [12]. As the load is further increased, one of the two samples begins to deform plastically. The load at which the plastic flow or yield begins depends on the yield point of the softer material in a simple tension test via a suitable yield criterion [10, 12]. Subsea connectors, for instance, experience up to 30-MPa-hydraulic pressure in a 300-m-deep seabed [35]. In the experiments, the performed contact pressure values were selected accordingly, which were within the elastic contact region for the XLPE samples (plastic flow after $44-\mathrm{MPa}$ pressure). Therefore, the next section covers only the elastic contacts.

3.2. Elastic Surface Contacts

In the light of the assumptions/simplifications made by Greenwood and Williamson [12] (bullet points in Section 3.1), Bhushan [10], showed that the apparent pressure p_a, mean real pressure p_r, (elastic) real area of contact A_{re}, the number of contact spots n, and mean asperity real area of contact as a function of separation d can be calculated. For this purpose, the contact between a plane and a nominally flat surface incorporating manifold spherically tipped asperities of the same radius β_m was considered with their peak heights represented by a probability density function of $p(z)$ as shown in Fig. 5. Contact mechanics of an individual cavity under a definite load is known from the Hertzian equations [12, 36], in which the contact radius a, area A_i, and load W_i are represented in terms of total peak displacement δ. Each elastic contact area for a peak displacement δ equals to $A_i = \pi\beta_m\delta$ and is circular with the radius $a = (\beta_m\delta)^{1/2}$ as depicted in Figs. 5 and 6; whereas, the load is given by $W_i = (4/3)E'\beta_m^{1/2}\delta^{3/2}$ [36].

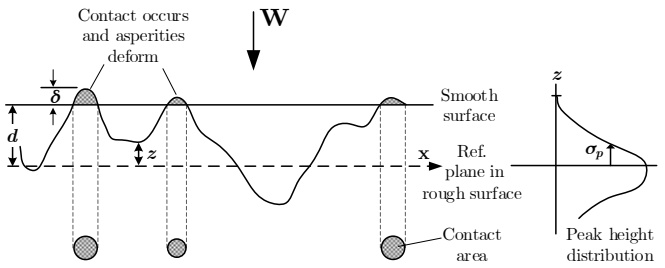

Figure 5: Schematic drawing of the contact between a rough surface and a smooth surface (rigid plane) [10].

When two surfaces are brought to contact until their reference planes are separated by d, contact spots will arise at any asperity whose height was formerly greater than d. Thus, the probability of having a contact at a given asperity height z is [10, 12, 36]:

$$P(z > d) = \int_d^\infty p(z)\,dz. \tag{3}$$

Moreover, if there are N asperities in total, the expected number of contacts n will then become

$$n = N\int_d^\infty p(z)\,dz. \tag{4}$$

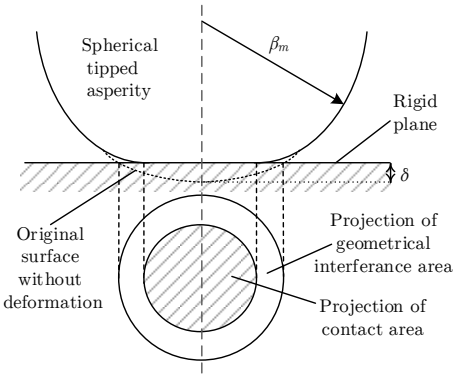

Figure 6: Contact area between a spherical asperity and a rigid plane, which is circular $\pi\beta_m\delta$ with the radius of $a = (\beta_m\delta)^{1/2}$ [14].

In addition, since the total displacement δ is equal to $z-d$, the total real area of contact becomes

$$A_{re} = \pi N\beta_m\int_d^\infty (z-d)p(z)\,dz. \tag{5}$$

Similarly, the expected total load ($W = NW_i$) is

$$W = \frac{4}{3}NE'\beta_m{}^{1/2}\int_d^\infty (z-d)^{3/2}p(z)\,dz, \tag{6}$$

where E' is the composite/effective elastic modulus (i.e., Young's modulus) of two materials in contact. Effective elastic modulus can be calculated by using elastic modulus of each surface in contact E, using the relation of

$$\frac{1}{E'} = \frac{1}{2}\left(\frac{1-v_1{}^2}{E_1} + \frac{1-v_2{}^2}{E_2}\right), \tag{7}$$

where E_1, v_1 and E_2, v_2 are the elastic modulus and Poisson's ratio of each material, respectively [21]. Note that Eqs. (3)–(6) hold for any type of surface peak-height distribution. For instance, in the case of Gaussian peak-height distribution:

$$p(z) = \frac{1}{\sigma\sqrt{2\pi}}\,e^{-\frac{1}{2}\left(\frac{z-\mu}{\sigma}\right)^2}, \tag{8}$$

where μ is expected value and σ^2 is variance of the random variable. Likewise, in case of an exponential asperity height distribution $p(z)$ becomes: $p(z) = \lambda e^{-\lambda z}$, where λ is the rate parameter provided that $\lambda > 0$.

Bhushan [8–10] manipulated the above formulae by introducing non-dimensional variables and standardized probability density functions, and then correlated the real area of contact A_{re} with the nominal contact area A_a in the elastic regime as:

$$A_{re} \cong 3.2\frac{p_a\,A_a}{E'\sqrt{\sigma_p/\beta_m}}, \tag{9}$$

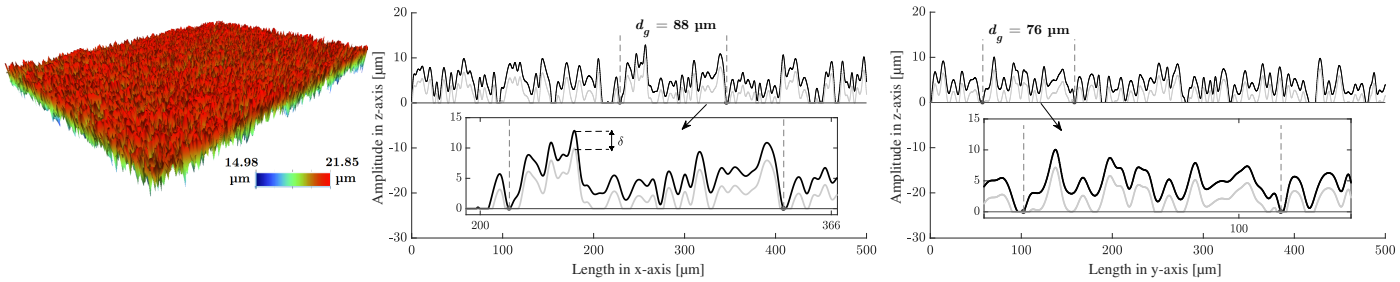

(a) (b) (c)

Figure 7: (a) Surface profilometer scan in $3-$D. Interface between an equivalent rough surface and a smooth plane: (b) Cursor $x-$axis data. (c) $y-$axis data.

where p_a is the apparent contact pressure in MPa and $p_a = W/A_a$ with W being the exerted force in N. The expected number of contact spots n is then yielded as

$$n = 1.21\eta A_a \left(\frac{p_a}{\eta\sigma_p\beta_m E' \sqrt{\sigma_p/\beta_m}} \right)^{0.88}, \qquad (10)$$

where η stands for the surface density of asperities [8–10]. With the help of Eqs. (9)–(10), the number of contacting points and the area that the contact spots take up as a fraction of the nominal contact area can be computed.

3.3. Average Size of Air-Filled Cavities

By further manipulating Eqs. (9)–(10), the total area the interfacial cavities occupy could also be computed. As stated in Section 3.1, equivalent rough surface simplifications do not affect the real area calculations and cause negligible differences [15]. In this study, we aim to develop a simple, two-dimensional contact surface model. This model will incorporate average cavity size for the sake of simplicity. Before further proceeding, the type of the cavities that exist on the polymer surfaces in high voltage equipment should be defined. For this purpose, the surface morphology of a polished XLPE sample is examined by following the methodology described in Section 5. Fig. 7(a) showcases the obtained three-dimensional surface profile whereas Figs. 7(b) and 7(c) depict two-dimensional profiles at the cursor position in $x-$ and $y-$axes, respectively. It should be noted that these profiles account for the interface between the equivalent rough surface and the smooth plane. The gray-solid lines represent the displaced asperity position under a heavier load, whereas the difference between the lines stands for the peak displacement δ in that exemplary case. The details on how to transform two rough surfaces into an equivalent rough surface and a smooth rigid plane could be found in [37].

What is observed in Figs. 7(b) and 7(c) is that the surface topographies both in the $x-$ and $y-$axes have similar distributions of peaks and valleys with comparable amplitudes i.e., isotropic, and the cavities formed in $xz-$ or $yz-$planes look like ellipsoids whose lengths parallel to the electric field are approximately $8-9$ times larger than those normal to the field. However, regardless of the cavity shape, the cavity size parallel to electric field component is of importance when determining the PDIE because the minimum value of PDIE is associated with the maximum path length in the field direction (critical avalanche length) [38].

In the light of the remarks above, the assumed interfacial cavity is illustrated in Fig. 8, whose tangential length d_g is much larger than the height h_z.

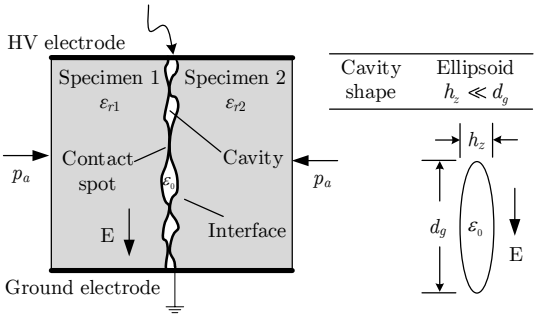

Figure 8: Defined cavity shape at the polymer interface.

As the average cavity shape is defined, the cavity area on the $xy-$plane should be determined at this stage. For simplicity, the projection area on the $xy-$plane is considered square with the side length d_g. A cavity in $3-$D can, thus, be envisaged as an ellipsoid whose height h_z is much smaller than its side lengths (d_g). On that account, d_g is calculated as follows:

$$\sum_{j=1}^{n} A_{cav,j} = A_a - A_{re}, \qquad (11a)$$

$$\overline{A}_{cav} = \frac{A_a - A_{re}}{n}, \qquad (11b)$$

$$d_g = \sqrt{\frac{A_a - A_{re}}{n}}, \qquad (12a)$$

$$d_g = \frac{\left(E' \sqrt{\frac{\sigma_p}{\beta_m}} - 3.2 p_a \right)^{0.5} \beta_m^{0.47}\, \sigma_p^{0.41}}{\sqrt{1.21}\, E'^{0.06}\, \eta^{0.06}\, p_a^{0.44}}, \qquad (12b)$$

where $A_{cav,j}$ and $\overline{A}_{cav}$ stand for the respective area of the j^{th} cavity and the average cavity area, respectively.

The three surface topography parameters σ_p, β_m and η in Eq. (12b) need to be determined to calculate the average cavity size d_g. For that purpose, the motif profiles

namely, roughness and waviness profiles, proposed in [39, 40], are used as explained in the following section.

3.4. Motif Profiles: Roughness and Waviness

Motif parameters offer a statistical description of asperity shapes and locations diffused on a broad range of micro-geometry from periodic to random profiles, where the primary asperities on isotropic rough surfaces are scrutinized by employing the summit and the radius of the altitude of each asperity [39]. Statistical analysis using probability density functions e.g., Gaussian or log-normal are used to describe each of these geometrical characteristics, where the distributions are redimensioned with the extracted characteristic values of the *roughness* and *waviness* parameters following the so-called *motif* procedure [39, 40].

The procedure in determining the motif parameters is described as follows as suggested in ISO 4287 [41]. First, the total surface profile is obtained using a surface characterization instrument. Second, a short-wave cut-off noise filter (λ_s) is applied to the total profile to obtain the primary profile. The roughness profile is then extracted by applying a band-pass filter with the short-wave cut-off wavelength λ_s and the long-wave cut-off wavelength λ_c to the primary profile P [42]. Likewise, a band-pass filter with the short-wave cutoff wavelength λ_c and the long-wave cutoff wavelength λ_f is applied to extract the waviness profile [42]. For proper selection of cut-off lengths, ISO 4287 [41] or ASME B46.1 [43] should be referred. Resulting profiles and motifs are schematically represented in Fig. 9.

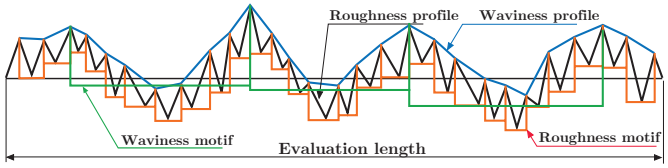

Figure 9: Schematic drawing of roughness and waviness motifs and extracted profiles from the primary profile [44].

A motif stands for a portion of the primary profile between the highest points of two local peaks of the profile, which are not necessarily adjacent [44]. The geometrical characteristics of a motif with the index i are as follows (see Fig. 10):

- H^i is the height difference between the left peak and the deepest valley;
- H^{i+1} is the height difference between the right peak and the deepest valley;
- Y^i is the mean height (of H^i and H^{i+1}) of the i^{th} motif;
- AY^i is the horizontal distance between the peaks of the i^{th} motif.

The following four conditions give the principal peaks and permit the calculation of roughness parameters of a surface consisting of a number of motifs:

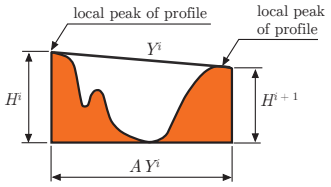

Figure 10: Length measured parallel to the general direction of the profile [44].

- Y is the average of the height values Y^i of the motifs (i.e., arithmetic mean asperity height);
- AY is the average of the width values AY^i of the motifs;
- SAY is the root mean square of the AY^i of the motifs.

Likewise, waviness parameters W and SW—the mean value and root-mean-square of the height values W_i of the waviness motifs, respectively—are determined following the same procedure using the waviness profile.

Belghith et al. [40] derived micro-geometry characteristics of the sum surface (i.e., an equivalent rough surface and a smooth surface) from each surface in contact. Thus, the parameters of the sum surface results from parameters of each surface with the subscripts 1 and 2 as [40]:

$$Y_{eq} = Y_1 + Y_2, \tag{13a}$$

$$W_{eq} = W_1 + W_2, \tag{13b}$$

$$AY_{eq} = \frac{1}{2}\left(AY_1 + AY_2\right), \tag{14a}$$

$$D = {}^1\!/_{AY_{eq}}, \tag{14b}$$

$$SAY_{eq} = \sqrt{SAY_1^2 + SAY_2^2}, \tag{15a}$$

$$SW_{eq} = \sqrt{SW_1^2 + SW_2^2}. \tag{15b}$$

Robbe-Valloire [39] revealed the surface characterization parameters of η, β_m and σ_p such that the density of asperities on a profile D are converted to the surface density of asperities η by using the correlation:

$$\eta = 1.2D^2. \tag{16}$$

The standard deviation of the distribution of the peak heights σ_p and the mean value of the summit radius β_m—considering two spherically shaped summits—are respectively given by

$$\sigma_p = 0.35\sqrt{W_{eq}^2 + SW_{eq}^2}, \tag{17}$$

$$\beta_m = \frac{AY_{eq}^2 + SAY_{eq}^2}{16Y_{eq}}. \tag{18}$$

To sum up, the motif parameters of the equivalent rough surface are computed using Eqs. (13a)-(15b). The resulting parameters are then substituted in Eqs. (17) and (18). As a remark, β_m and σ_p of the sum surface could be calculated in an alternative way. Eq. (18) can be utilized

to calculate β_{m1} and β_{m2} separately by using the Y, AY, and SAY motif parameters of each surface. The resulting β_m is then computed using Eq. (1). A similar procedure is followed for σ_p, too.

As Leach [42] suggested, the arithmetic mean asperity height Y represents an overall measure of the surface texture, and it can be used in identifying different rough surfaces under consideration. Thus, Y or Y_{eq} will be utilized in the first place when a brief comparison is exercised in the results.

4. Hypothesis

The electric field at which the breakdown strength of the gas in the cavity is exceeded is defined as the cavity discharge inception field strength E_i (i.e., PDIE). Under a homogeneous electric field, the PDIE of an air-filled cavity is characterized by the Paschen's curve for air [7, 18]. The portion of the Paschen's curve that covers a cavity size within $10\,\mu\text{m} - 1\,\text{mm}$ is shown in Fig. 11 for five different air-pressures confined in the cavity (p_c). The curves suggest a reduced inception field strength as the cavity size increases.

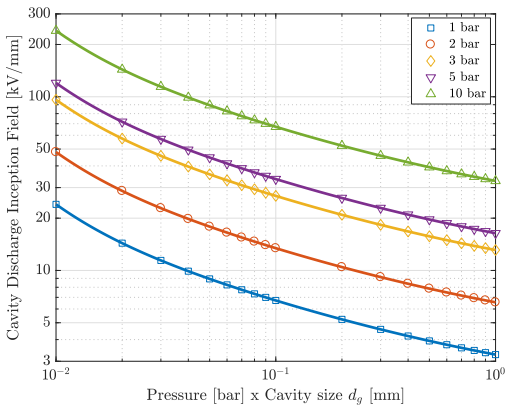

Figure 11: The Paschen's curve for air under various air pressure. (1 bar = 0.1 MPa.)

The curves in Fig. 11 are plotted by using the following polynomial fit equation to the empirical data:

$$E_i(p_c, d_g) = A\frac{p_0/p_c}{{d_g}^2} + B(p_c/p_0) + \frac{C}{d_g} + D\sqrt{\frac{p_c/p_0}{d_g}} \quad (19)$$

where $p_0 = 1\,\text{bar}$, $\text{A} = 0.00101\,\text{kV}\cdot\text{mm}$, $\text{B} = 2.4\,\text{kV/mm}$, $\text{C} = -0.0097\,\text{kV}$, $\text{D} = 2.244\,\text{kV}\cdot\text{mm}^{-0.5}$ [18].

Our previous work [7, 45–48] indicated that the pressure in the gas-filled cavities settled around the ambient pressure (ester-filled container exposed to atmospheric pressure); otherwise, much higher interfacial BDS values would have resulted in according to ideal gas theory. In other words, initially compressed air in the cavities is probably squeezed out due to the cavity-rich surface texture as can be envisaged from the conceptual sketch in Fig. 1(b). In this case, they are vented to the surroundings, and the pressure inside of the cavities remains constant at the ambient pressure i.e., $p_c \simeq 1\,\text{bar}$.

The possibility of vented channels coexisting with numerous interlocked minute cavities, in which the air pressure is likely to be higher than 1 bar, should not be ruled out [46]. The inception field strength of a vented cavity is, however, much lower than that of an interlocked cavity according to Paschen's law. Thereby, in our hypothesis, we assume that the vented cavities are the principal governing mechanism in the interfacial breakdown phenomenon.

A flashover in a cavity at the interface is analogous to the onset of the interfacial partial discharge (PD) activity [45]. When PD starts, discharge extends from one end of the cavity surface and traverses through the gas-filled cavity and reaches the other end of the cavity surface. Hence, it only bridges the cavity not the whole insulation between electrodes. Whether discharges in these cavities can cause a complete flashover across the interface or the duration until a PD evolves to a complete flashover depends upon electric treeing resistance of the insulation and is not covered herein. However, there is voltage and time difference between the PDIE and the BDS since the former is the initial stage (cause) whereas the latter is the ultimate consequence (effect) [37]. This is because the process depends on the factors such as availability of a free electron to start the avalanche process, the energy of the electron, the field strength in the cavity accelerating the electrons, and so forth [18]. Thus, we will seek a simple relationship between PDIE and BDS as follows.

To correlate cavity discharge and interfacial breakdown phenomenon, we hypothesize that experimentally obtained interfacial BDS (i.e., applied field stress by the power source—BDS_{exp}) is linearly proportional to the E_i:

$$\text{BDS}_{\text{exp}} = \alpha \cdot \frac{E_i}{f}, \quad (20)$$

where α is a numerical coefficient. As a remark, the electric field strength in the air-filled cavities is enhanced by a factor f, depending on the cavity shape since the permittivity of air is less than the permittivity of the bulk material [38, 49]. Thus, E_i is divided by the enhancement factor f to calculate the field strength in the bulk insulation i.e., scaled PDIE. For the defined cavity shape in Section 3.3, $f \approx 1$ [38]. It is important to note that, if the electric field was applied perpendicularly rather than tangentially in Fig. 8, the factor would become $f \approx \epsilon_r$, where ϵ_r is the dielectric permittivity of the bulk insulation—$\epsilon_r = 2.3$ for XLPE. As a remark, since the statistical model developed in this paper employs the average cavity size, discharges take place in the cavities with the size of equal to or greater than d_g in theory, where d_g accounts for the tangential length of the cavity. In the results section, the strength and the limitations of the tribological contact model will be assessed via the computed α values.

5. Experimental Procedure

5.1. Sample Preparation: Cutting and Polishing

Samples were obtained from a commercial XLPE-insulated 145 kV power cable. Each sample was cut in rectangular prisms with the dimensions of 55 mm x 30 mm x 4 mm, where the nominal contact area A_a is 4 mm x 55 mm as shown in Fig. 12. We then polished the contact surfaces of the samples using STRUERS Abramin tabletop, rotating grinding machine. Four different sandpapers of different grits (#180, #500, #1000, and #2400) were used. The specimens were fixed on a steel rotating disk, and a round-SiC sandpaper of the desired grit was placed on the rotating plane (see [45]). The speed of the rotating plane was set to 150 rpm, and the force pressing the steel disk towards sandpaper was fixed to 300 N during polishing of all the samples, ensuring that surfaces underwent the same procedure. The speed and the force values were determined based on a number of initial tests.

The instrument polished the samples for $2-3$ minutes with a continuous flow of water to remove any by-products and polymer remnants, and to avoid heating caused by friction. Subsequently, the samples were rinsed in tap water and were left to dry in air. Dry samples were then cleaned using filtered compressed air before they were washed briefly in isopropanol. Finally, the samples were left to dry again at room temperature.

5.2. Sample Characterization

5.2.1. Elastic Modulus Measurement

The elastic modulus (Young's modulus) of five virgin XLPE samples were measured using Lloyd LR5K gauge under tensile testing that makes use of the initial slope of the obtained stress-strain curve following the ASTM D 790 standard [50]. Next, the effective elastic modulus E' of the mated XLPE-XLPE interface was calculated using Eq.(7).

5.2.2. Surface Roughness Characterization

A 3D-optical profilometer (Bruker Contour GT – K [51]) was used to characterize the surface topography of the polished surfaces of the samples. 50X magnification was opted with 0.2 μm lateral sampling resolution and 3 nm vertical resolution by following the detailed study performed in [52]. Scanned surface area was 125 μm x 95 μm. Several scans were performed at different sections to examine consistency or any scatter.

5.3. High Voltage Testing

5.3.1. Mechanical Test Setup

The test set-up with the dimensions of the core components is demonstrated in Fig. 12. There, two samples were positioned on top of each other under dry ambient conditions and were placed between two Rogowski-profile electrodes. The width of the contact surface i.e., interface is 4 mm. Then, the contact pressure was applied before filling the test chamber with synthetic ester (Midel 7131) to avoid the ester from penetrating the interface. The interfacial BDS against ester penetration was tested in [7], and the samples assembled in the ester yielded much higher BDSs than dry-mated samples that had proved that the ester penetration was not at stake or its effect was negligible on the BDS.

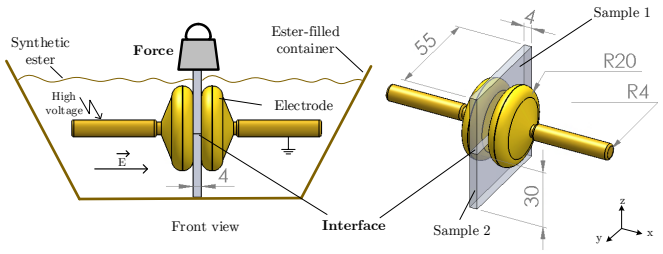

Figure 12: The simplified sketch of the mechanical test setup. Dimensions are given in mm. Details of the mechanical setup is shown in [37, 45].

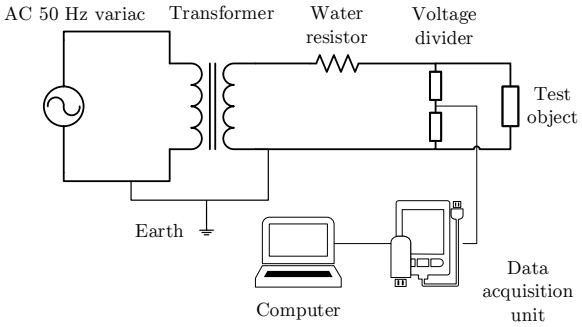

Figure 13: The sketch of the overall electrical test setup.

5.3.2. Setup for AC Breakdown Tests

Fig. 13 shows the complete electrical test setup. A 50-Hz variac ($0-230$ V) was used to energize the primary side of a 100 kV transformer, generating AC ramp voltage on the secondary winding at the rate of 1 kV/s. A water resistor was used to limit the breakdown current. Also, a voltage divider was connected in parallel to measure the applied voltage recorded by PC via a data acquisition unit.

5.3.3. Test Procedure & Data Handling

The required contact pressure was exerted using weights ranging between $11-26$ kg as illustrated in Fig. 12. The average contact pressure is then calculated using $p_a = F/A_a$, where F is the exerted contact force in N and A_a is the interface area in m^2 (4 mm x 55 mm).

Each set of experiments was composed of eight repeated tests using a virgin pair of samples each time. The obtained results were statistically evaluated using the two-parameter Weibull distribution [18, 53]. For further evaluation, the nominal value of the Weibull (i.e. 63.2 percentile) with the 90% confidence interval was used. Goodness-of-fit in each case was tested by following the guidelines in [53].

6. Results and Discussion

6.1. Experimental Results

6.1.1. Elastic Modulus

Average of five Young's modulus measurements of XLPE samples was calculated to be 200 MPa with the Poisson's ratio 0.46, yielding a resulting effective/composite elastic modulus of 226 MPa for the XLPE-XLPE interface.

6.1.2. Surface Characterization

The calculated roughness and waviness motif parameters of the XLPE-XLPE sum surface are shown in Table 1. In addition, Table 2 contains the obtained surface characterization parameters of σ_p, β_m, and η following the procedure described in Section 3.4. Extracted surface roughness and waviness profiles are also shown in Fig. 14.

Table 1: Motif parameters of the XLPE-XLPE interface.

Interface	Roughness [μm]			Waviness [μm]	
	Y_{eq}	AY_{eq}	SAY_{eq}	W_{eq}	SW_{eq}
#180	17.79	19.30	13.97	11.39	9.80
#500	5.65	20.61	12.38	5.43	4.87
#1000	1.98	21.47	13.23	1.25	1.08
#2400	0.50	27.59	13.44	0.34	0.35

Table 2: Surface characterization parameters.

Interface	σ_p [μm]	β_m [μm]	η [μm]
#180	5.26	1.94	$3.22 \cdot 10^{15}$
#500	2.55	6.39	$2.83 \cdot 10^{15}$
#1000	0.58	19.91	$2.64 \cdot 10^{15}$
#2400	0.17	118.19	$1.58 \cdot 10^{15}$

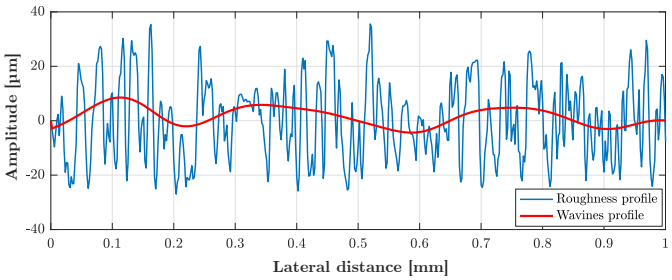

Figure 14: Obtained roughness and waviness profiles by the optical profilometer. Filters employed with the following cut-off lengths: $\lambda_s = 8\,\mu$m, $\lambda_c = 0.08$ mm, $\lambda_f = 0.25$ mm.

6.1.3. AC Breakdown Tests

Experimental results displaying the influence of the surface roughness on the interfacial BDS under 0.5, 0.86, and 1.16 MPa contact pressures are shown in Fig. 15. 63.2 percentile values are plotted with their 90% confidence intervals (CI); whereas, each curve represents a different roughness degree. As a remark, Y_{eq} in Table 1 stands for the aggregate roughness of the XLPE-XLPE interface accounting for the roughness of the each XLPE surface as depicted in Eq. (13a). The results suggest, in each case, that an increased roughness (i.e., higher Y_{eq}) results in an reduced BDS whereas an increased contact pressure results in an increased BDS as evident in Fig. 15. Table 3 supplies the quantitative data points for Fig. 15.

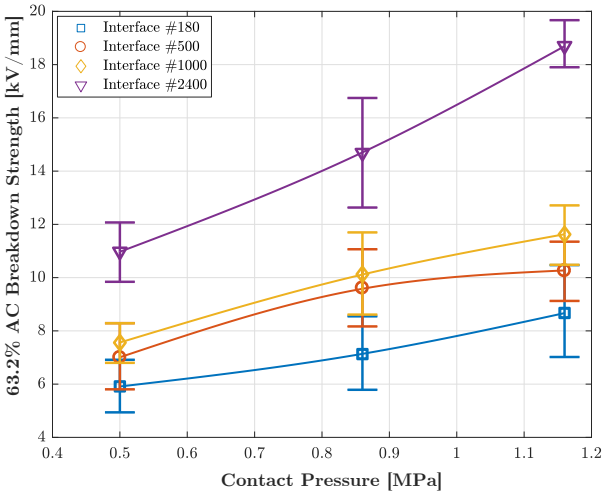

Figure 15: The experimental BDS data vs. contact pressure. The errorbars stand for the 90% CI; whereas, the markers point the 63.2 percentile.

Table 3: Overview of the experimental results.

XLPE-XLPE Interface	63.2% BDS [kV/mm]		
	0.5 MPa	0.86 MPa	1.16 MPa
#180	5.92	7.13	8.67
#500	6.99	9.61	10.26
#1000	7.56	10.13	11.62
#2400	10.98	14.69	18.70

The 63.2 percentile BDS in the case of the surface polished by #2400 is nearly twice as high as that of in the case of #180 under each contact pressure. To be exact, as Y_{eq} is reduced by a factor of 36 from #180 to #2400, the BDS increases by a factor ranging in $1.85 - 2.15$ at $p_a = 0.5 - 1.16$ MPa. The improvement in the 63.2 percentile BDS from #180 to #500 or from #180 to #1000 is; however, not as notable, only by a factor of $1.2 - 1.3$. The rate of change in the BDS from #1000 to #2400 culminates under all pressures as evident in Fig. 15, where the highest increase is detected at 1.16 MPa by a factor of 1.6. It can, thus, be inferred that the smoothness of the surface can play as vital a role as the contact pressure in improving the BDS of the interfaces under dry-mated conditions.

As the pressure is raised from 0.5 MPa to 1.16 MPa, the 63.2 percentile BDS becomes 1.4 times as high for #180 ($Y_{eq} = 17.79\,\mu$m); whereas, it increases by a factor of 1.7 for #2400 ($Y_{eq} = 0.50\,\mu$m). Eq. (12b) supports the discussion herein such that the increased interfacial pressure reduces the size of the air-filled cavities at the considered surface, where the biggest change in BDS by a factor of 1.7 was observed in the case of the smoothest surface. However, despite the increased contact pressure, there exist BDS values of similar magnitude at the same pressure especially in the case of the roughest surface (#180) as can

Table 4: Tabulated output of the proposed contact model.

Param. / Interface	0.5 MPa			0.86 MPa			1.16 MPa		
	A_{re}/A_a [%]	n [1/mm^2]	d_g [μm]	A_{re}/A_a [%]	n [1/mm^2]	d_g [μm]	A_{re}/A_a [%]	n [1/mm^2]	d_g [μm]
#180	0.41	221	75.6	0.70	357	59.7	0.94	464	52.1
#500	1.06	335	61.3	1.82	540	48.1	2.45	703	42.0
#1000	3.91	1433	29.2	6.73	2309	22.7	9.08	3005	19.6
#2400	17.55	3082	18.5	30.18	4967	13.4	40.71	6464	10.8

be seen in Fig. 15. The overlapping portions of the bars, on the other hand, tend to dwindle as the surface roughness decreases. In the case of the smoothest surface, there are not any coincident BDS values as seen in Fig. 15.

6.2. Correlation between PDIE and BDS

The resulting variables of the contact model—A_{re}, n, and the average cavity size d_g— are tabulated in Table 4. For a wholesome assessment, the sizes of average cavities are calculated with two-sigma significance (i.e. equivalent to 95% CI [54]) via the standard deviation of the asperity radius σ_p. Thus, an estimated cavity size is represented with its 95% CI by a hatched-region while the markers in Fig. 16 signify the experimentally applied pressure values for reference.

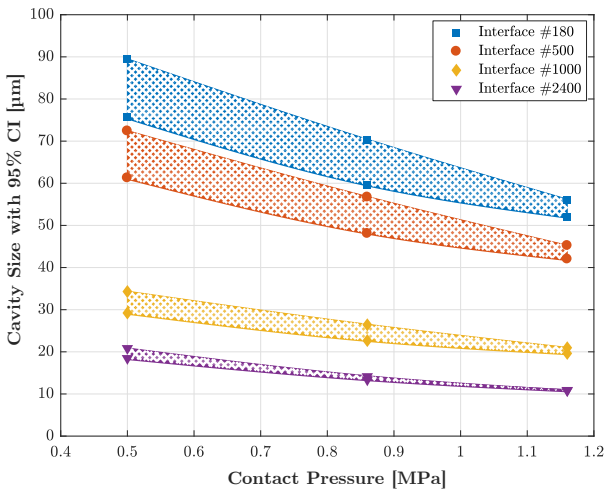

Figure 16: Calculated cavity size via (12b) plotted against the applied contact pressure.

It is interesting to discover the contact model correlating with the experimental results to a significant extent despite a number of assumptions and simplifications made in the modeling. First of all, A_{re}/A_a data in Table 4 suggest that the real area of contact considerably augments as the surface roughness decreases. The most significant change in A_{re}/A_a is observed from #1000 to #2400 by a factor of 4.5 under each contact pressure, which accords well with the experimental data shown in Fig. 15. Likewise, the average cavity size d_g decreases by a factor of $4.08 - 4.82$ from the roughest interface #180 to the smoothest interface #2400 as the contact pressure p_a is increased from 0.5 MPa to 1.16 MPa. The bottom line is expanded real contact area results in a substantial increase in the number of contact spots n (can be envisaged in Fig. 7 as well) and hence a reduced average cavity size.

Based on the hypothesis in Section 4, the scaled PDIE values (E_i/f) are calculated and are plotted in Fig. 17 alongside the experimentally obtained BDS values. Each E_i/f data-set is computed by substituting the d_g data-set (in Fig. 16) into Eq. (19). For convenience, E_i/f and scaled PDIE are used interchangeably. Also, the scaled PDIE and the experimental BDS data with their corresponding CIs are plotted versus equivalent mean asperity height Y_{eq} in Fig. 18, which additionally incorporates the CIs of the experimental BDS values.

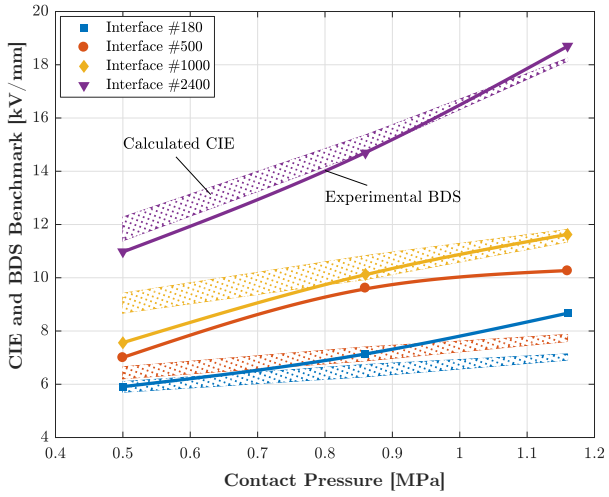

Figure 17: Experimental BDS data vs. scaled theoretical PDIE (E_i/f) against contact pressure. (Solid lines: Experimental data. Hatched-regions: Calculated PDIE via Eqs. (12b), (19) and (20).)

As observed in Fig. 17, the smoother the surface, the closer the affinity between the cavity discharge inception field and the experimental BDS data, especially at higher contact pressures. Besides, the E_i/f values are lower than the experimental data in the case of rougher surfaces toward higher pressures (see Fig. 17). Likewise, E_i/f values tend to deviate from the experimental data in the cases of the two roughest surfaces (#180 and #500) as the pressure is raised from 0.5 MPa to 1.16 MPa. In contrast, an opposite tendency is observed in the case of smoother surfaces (#1000 and #2400). The resulting α coefficients in Eq. (20) are plotted in Fig. 19, where α ranges from 0.8 to 1.05 at 0.5 MPa while it spans $0.98 - 1.3$ at 1.16 MPa. As seen, α digresses from unity by 30% at most toward

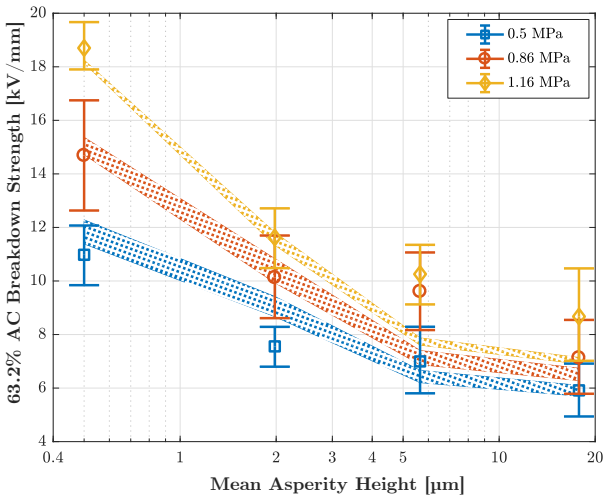

Figure 18: Experimental BDS vs. scaled PDIE: (a) 0.5 MPa. (b) 0.86 MPa. (c) 1.16 MPa.

higher p_a, however when the CIs in Fig. 18 are considered, the range even reduces to $0.86 - 1.05$. This close affinity between the cavity discharge and the interface breakdown suggests that the interfacial breakdown phenomenon is strongly governed by the cavity discharge.

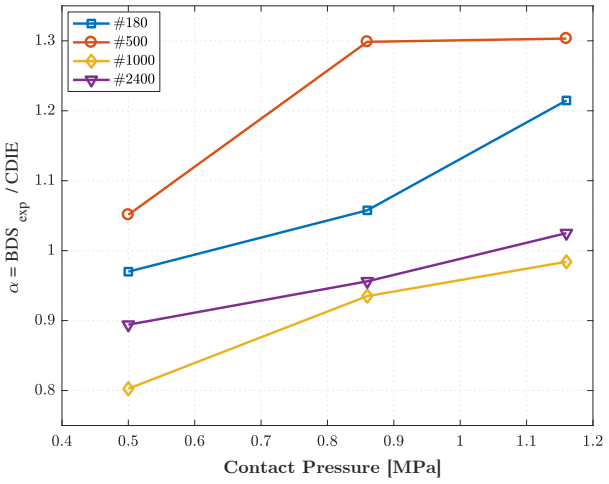

Figure 19: α vs. contact pressure under four different roughnesses.

In the light of the discussion herein, the following remarks are made. Due to normally distributed cavity peaks and heights, there are at least a number of cavities larger than the average-sized cavities, in which the PD activity presumably commences first whereas there is still no PD activity in the average-sized cavities. Thereby, depending on the number and size of such larger cavities, the governance of the cavity discharges on the interfacial breakdown phenomenon presumably diminishes. Consequently, an improved tribological contact model that incorporates the influence of the size and number of the largest cavities might perform better. Furthermore, testing different polymers with different modulus in addition to the analysis performed in this work could help improve the model. Last but not least, our unpublished results (to be found in [37] eventually), where we achieved monitoring discharge activity at the interface using a CCD camera setup, suggested that the discharge activity first commences in the cavities. Then, when the cavities are completely ionized, discharge extends from one end of the cavity surface and traverses the gas-filled cavity. The interfacial breakdown then follows eventually. The magnitude and phase of the discharges were also measured via a PD measuring unit (Omicron MPD600). Consequently, all these results offer a promising potential to define a more complex correlation between the cavity discharge and the interfacial breakdown strength for future work.

7. Conclusion

A novel contact surface model for solid dielectric materials was proposed, and the results generated by the model (PDIE) were verified and correlated with the experimental data. The calculated average cavity size decreased by a factor of $4.08 - 4.82$ from the roughest to the smoothest surface, that in turn yielded increased PDIEs by a factor of $2.01 - 2.56$. Likewise, the experimentally obtained BDS values augmented by a factor of $1.4 - 1.7$ when the contact pressure was increased from 0.5 MPa to 1.16 MPa. The calculated PDIE was correlated with the experimental BDS via a linear correlation coefficient, which varied between $0.8 - 1.3$. Taking the 90% CIs into account has even reduced the range to $0.86 - 1.05$. This close affinity between the cavity discharge and the interface breakdown suggests that the cavity discharge governs the interfacial breakdown phenomenon to a significant extent. To our knowledge, this model is one of the first models blending tribology and high voltage engineering in the literature. Because of the satisfactory agreement between the model outputs and experimental results, we believe that the model deserves further studies.

Acknowledgment

This work is funded by the project "High Voltage Subsea Connections (SUBCONN)." The project is supported by The Research Council of Norway (Project No. 228344/E30), and by the following industrial partners: ABB AS, Aker Solutions AS, Deutsch Offshore, Chevron Norge AS, Det Norske Oljeselskap ASA, Nexans Norway AS, Shell Technology Norway AS and Equinor ASA (formerly [Statoil Petroleum AS]).

References

[1] D. Kunze, B. Parmigiani, R. Schroth, E. GocNenbach, Macroscopic internal interfaces in high voltage cable accessories, in: CIGRE, 2000, pp. 15–203.

[2] D. Fournier, L. Lamarre, Interfacial breakdown phenomena between two epdm surfaces, in: Proc. 6th Int. Conf. Dielectr. Mater. Meas. App., 1994, pp. 330–333.

[3] E. Peschke, R. von Olshausen, Cable systems for high and extra-high voltage: development, manufacture, testing, installation and operation of cables and their accessories, Wiley-VCH, 1999.

[4] B. Du, L. Gu, Effects of interfacial pressure on tracking failure between XLPE and silicon rubber, IEEE Trans. Dielectr. Electr. Insul. 17 (6) (2010) pp. 1922–1930.

[5] B. Du, X. Zhu, L. Gu, H. Liu, Effect of surface smoothness on tracking mechanism in XLPE-si-rubber interfaces, IEEE Trans. Dielectr. Electr. Insul. 18 (1) (2011) pp. 176–181.

[6] T. Takahashi, T. Okamoto, Y. Ohki, K. Shibata, Breakdown strength at the interface between epoxy resin and silicone rubber-a basic study for the development of all solid insulation, IEEE Trans. Dielectr. Electr. Insul. 12 (4) (2005) pp. 719–724.

[7] E. Kantar, D. Panagiotopoulos, E. Ildstad, Factors influencing the tangential AC breakdown strength of solid-solid interfaces, IEEE Trans. Dielectr. Electr. Insul. 23 (3) (2016) pp. 1778–1788.

[8] B. Bhushan, Principles and applications of tribology, John Wiley & Sons, 2013.

[9] B. Bhushan, Analysis of the real area of contact between a polymeric magnetic medium and a rigid surface, J. Tribol. 106 (1) (1984) pp. 26–34.

[10] B. Bhushan, Contact mechanics of rough surfaces in tribology: multiple asperity contact, Tribol. Letters 4 (1) (1998) pp. 1–35.

[11] B. Bhushan, X. Tian, A numerical three-dimensional model for the contact of rough surfaces by variational principle, ASME J. Tribol. 118 (1996) pp. 33–42.

[12] J. Greenwood, J. Williamson, Contact of nominally flat surfaces, in: Proc. R. Soc. A, Vol. 295, The Royal Society, 1966, pp. 300–319.

[13] J. Williamson, J. Pullen, R. Hunt, The shape of solid surfaces, ASME Surf. Mechanics 9 (1969) pp. 334.

[14] J. Greenwood, The area of contact between rough surfaces and flats, J. Lubrication Tech. 89 (1) (1967) pp. 81–87.

[15] J. Greenwood, J. Tripp, The contact of two nominally flat rough surfaces, Proc. Instit. Mech. Eng. 185 (1) (1970) pp. 625–633.

[16] E. Kantar, S. Hvidsten, F. Mauseth, E. Ildstad, Tangential AC breakdown strength of solid-solid interfaces considering surface roughness, in: IEEE Conf. Electr. Insul. and Dielectr. Phen. (CEIDP), Vol. 1, 2017, pp. 580–583.

[17] D. Fournier, Effect of the surface roughness on interfacial breakdown between two dielectric surfaces, in: Proc. Conf. IEEE Int. Sympos. Elect. Insul., Vol. 2, IEEE, 1996, pp. 699–702.

[18] L. A. Dissado, J. C. Fothergill, Electrical degradation and breakdown in polymers, Vol. 9, IET, 1992.

[19] J. CIGRE, 21/15: Interfaces in accessories for extruded hv and ehv cables, Electra (203) (2002) pp. 53–59.

[20] F. M. Borodich, A. Pepelyshev, O. Savencu, Statistical approaches to description of rough engineering surfaces at nano and microscales, Tribol. Int. 103 (2016) pp. 197–207.

[21] A. Almqvist, On the effects of surface roughness in lubrication, Ph.D. thesis, Luleå tekniska universitet (2006).

[22] V. Zhuravlev, On the question of theoretical justification of the Amontons-Coulomb law for friction of unlubricated surfaces, Proc. IMechE Part J. 221 (8) (2007) pp. 895–898.

[23] K. Johnson, Non-hertzian contact of elastic spheres, IUTAM Symposium (Eds. A.D. de Pater and J.J. Kalker) (1975) pp. 26–40.

[24] J. Greenwood, Surface modelling in tribology, App. surf. model. (Eds C. F. M. Creasy and C. Craggs) (1990) pp. 61–75.

[25] F. Borodich, Introduction to Zhuravlev's historical paper: On the question of theoretical justification of the Amontons-Coulomb law for friction of unlubricated surfaces, Proc. IMechE Part J. 221 (8) (2007) pp. 893–895.

[26] J. Archard, Elastic deformation and the laws of friction, in: Proc. R. Soc. A, Vol. 243, The Royal Society, 1957, pp. 190–205.

[27] F. Borodich, D. Onishchenko, Similarity and fractality in the modelling of roughness by a multilevel profile with hierarchical structure, Int. J. Solids and Structures 36 (17) (1999) pp. 2585–2612.

[28] P. R. Nayak, Random process model of rough surfaces, J. of Lubrication Tech. 93 (3) (1971) pp. 398–407. doi:10.1115/1.3451608.

[29] D. J. Whitehouse, J. Archard, The properties of random surfaces of significance in their contact, in: Proc. R. Soc. Lond A., Vol. 316, The Royal Society, 1970, pp. 97–121.

[30] M. Ciavarella, G. Demelio, J. Barber, Y. H. Jang, Linear elastic contact of the weierstrass profile, in: Proc. R. Soc. Lond A., Vol. 456, The Royal Society, 2000, pp. 387–405.

[31] A. Majumdar, B. Bhushan, Fractal model of elastic-plastic contact between rough surfaces, J. Tribology 113 (1) (1991) pp. 1–11.

[32] D. Whitehouse, Fractal or fiction, Wear 249 (5–6) (2001) pp. 345–353.

[33] M. O'Callaghan, M. Cameron, Static contact under load between nominally flat surfaces in which deformation is purely elastic, Wear 36 (1) (1976) pp. 79–97.

[34] H. Francis, Application of spherical indentation mechanics to reversible and irreversible contact between rough surfaces, Wear 45 (2) (1977) pp. 221–269.

[35] S. Midttveit, B. Monsen, S. Frydenlund, K. Stenevik, et al., SS on implications of subsea processing power distribution-subsea power systems—a key enabler for subsea processing, in: Offshore Technol. Conf., Offshore Technol. Conf., 2010.

[36] J. A. Greenwood, J. H. Tripp, The elastic contact of rough spheres, J. Appl. Mechanics 34 (1) (1967) pp. 153–159.

[37] E. Kantar, Characterization of Longitudinal AC Electric Breakdown Strength of Solid Dielectric Interfaces, Ph.D. thesis, Norwegian University of Science and Technology (2018).

[38] G. C. Crichton, P. W. Karlsson, A. Pedersen, Partial discharges in ellipsoidal and spheroidal voids, IEEE Trans. Electr. Insul. 24 (2) (1989) pp. 335–342.

[39] F. Robbe-Valloire, Statistical analysis of asperities on a rough surface, Wear 249 (5) (2001) pp. 401–408.

[40] S. Belghith, S. Mezlini, H. BelhadjSalah, J.-L. Ligier, Modeling of contact between rough surfaces using homogenisation technique, Comptes Rendus Mécanique 338 (1) (2010) pp. 48–61.

[41] Geometrical Product Specifications (GPS)–Surface Texture: Profile Method–Terms, Definitions and Surface Texture Parameters, ISO, 2000.

[42] R. Leach, Characterisation of areal surface texture, Springer, 2013.

[43] ANSI, Surface texture (surface roughness, waviness, and lay). B46. 1, The American Society Mechanical Eng., 1985.

[44] TOKYO SEIMISU, Surface texture contour measuring instruments, http://www.inspectionengineering.com/Images/SurfaceFinishExplain.pdf.

[45] E. Kantar, S. Hvidsten, F. Mauseth, E. Ildstad, Longitudinal AC breakdown voltage of XLPE-XLPE interfaces considering surface roughness and pressure, IEEE Trans. Dielectr. Electr. Insul. 24 (5) (2017) pp. 3047–3054.

[46] E. Kantar, F. Mauseth, E. Ildstad, Interfacial breakdown between dielectric surfaces determined by gas discharge, in: IEEE Conf. Electr. Insul. and Dielectr. Phen. (CEIDP), Vol. 1, 2017, pp. 556–559.

[47] E. Kantar, E. Ildstad, Modeling longitudinal breakdown strength of solid-solid interfaces using contact theory, in: 2016 IEEE Int. Conf. on Dielec. (ICD), Vol. 1, 2016, pp. 398–401.

[48] E. Kantar, S. Hvidsten, E. Ildstad, Examination of longitudinal AC breakdown strength of dielectric surfaces as a function of elastic modulus, Proc. Nordic Insul. Sympos. 25 (1) (2017) pp. 1–5. doi:10.5324/nordis.v0i25.2360.

[49] H. A. Illias, Measurement and simulation of partial discharges within a spherical cavity in a solid dielectric material, Ph.D. thesis, University of Southampton (2011).

[50] ASTM D20.10, Standard test methods for flexural properties of unreinforced and reinforced plastics and electrical insulating materials D790–17, 2007.

[51] Bruker, ContourGT-K 3D Optical Microscope, https://www.bruker.com/products/surface-and-dimensional-analysis/3d-optical-microscopes/contourgt-k/overview.html.

[52] C. Y. Poon, B. Bhushan, Comparison of surface roughness measurements by stylus profiler, AFM and non-contact optical profiler, Wear 190 (1) (1995) pp. 76–88.

[53] IEC/IEEE guide for the statistical analysis of electrical insulation breakdown data (adoption of ieee std 930-2004), IEC 62539 First Edition 2007-07 IEEE 930 (2007) pp. 1–53.

[54] A. Leon-Garcia, Probability, Statistics, and Random Processes for Electrical Engineering, Pearson Education, 2017.